Article

Li$_4$*Ln*[PS$_4$]$_2$Cl: Chloride-Containing Lithium Thiophosphates with Lanthanoid Participation (*Ln* = Pr, Nd and Sm)

Pia L. Lange [1] , Sebastian Betto [2] , Sabine Strobel [1], Robert E. Dinnebier [2] and Thomas Schleid [1,*]

1   Institute for Inorganic Chemistry, University of Stuttgart, Pfaffenwaldring 55, 70569 Stuttgart, Germany
2   Max Planck Institute for Solid State Research, Heisenbergstraße 1, 70569 Stuttgart, Germany
*   Correspondence: schleid@iac.uni-stuttgart.de

Abstract: The synthesis and structural analysis of three new chloride-containing lithium thiophosphates(V) Li$_4$*Ln*[PS$_4$]$_2$Cl with trivalent lanthanoids (*Ln* = Pr, Nd and Sm) are presented and discussed. Single crystals of Li$_4$Sm[PS$_4$]$_2$Cl were obtained and used for crystal structure determination by applying X-ray diffraction. The other compounds were found to crystallize isotypically in the monoclinic space group $C2/c$. Thus, Li$_4$Sm[PS$_4$]$_2$Cl (a = 2089.31(12) pm, b = 1579.69(9) pm, c = 1309.04(8) pm, β = 109.978(3)°, Z = 12) was used as a representative model to further describe the crystal structure in detail since Li$_4$Pr[PS$_4$]$_2$Cl and Li$_4$Nd[PS$_4$]$_2$Cl were confirmed to be isotypic using powder X-ray diffraction measurements (PXRD). In all cases, a trigonal structure in the space group $R\overline{3}$ (e.g., a = 1579.67(9) pm, c = 2818.36(16) pm, c/a = 1.784, Z = 18, for Li$_4$Sm[PS$_4$]$_2$Cl) displaying almost identical building units worked initially misleadingly. The structure refinement of Li$_4$Sm[PS$_4$]$_2$Cl revealed bicapped trigonal prisms of sulfur atoms coordinating the two crystallographically distinct (Sm1)$^{3+}$ and (Sm2)$^{3+}$ cations, which are further coordinated by four anionic [PS$_4$]$^{3-}$ tetrahedra. The compounds also contain chloride anions residing within channel-like pores made of [PS$_4$]$^{3-}$ units. Eight different sites for Li$^+$ cations were identified with various coordination environments (*C.N.* = 4–6) with respect to chlorine and sulfur. EDXS measurements supported the stoichiometric formula of Li$_4$*Ln*[PS$_4$]$_2$Cl, and diffuse reflectance spectroscopy revealed optical band gaps of 2.69 eV, 3.52 eV, and 3.49 eV for Li$_4$Sm[PS$_4$]$_2$Cl, Li$_4$Nd[PS$_4$]$_2$Cl, and Li$_4$Pr[PS$_4$]$_2$Cl, respectively. The activation energy for Li$^+$-cation mobility in Li$_4$Sm[PS$_4$]$_2$Cl was calculated as E_a(Li$^+$) = 0.88 eV using BVEL, which indicates potential as a Li$^+$-cation conductor.

Keywords: crystal structure; lanthanoids; thiophosphates; lithium; chlorides

1. Introduction

Lithium-containing ternary *ortho*-thiophosphates(V) with their complex [PS$_4$]$^{3-}$ anions were first reported in 1982 [1]. A whole lot more compounds and structures are known for quaternary derivatives, whether by introducing new cations, such as rare-earth metals [2], for example, or by adding further anions, like halogenides [3]. Li$_6$PS$_5$Cl [4] (=Li$_6$[PS$_4$]SCl) derived from argyrodite (Ag$_8$[GeS$_4$]S$_2$) [5], a silver mineral, where the halogenide anions build a tetrahedral close packing with the [PS$_4$]$^{3-}$ units in the tetrahedral voids [6], is a promising material for Li$^+$-cation conducting all solid-state batteries as electrolyte [6]. Compounds like these often provide enough flexibility by being disordered to allow for ion mobility within their structures.

The search for a suitable solid electrolyte for all solid-state lithium-ion batteries is fueling the progress in this field of research. Beginning with the ternary Li$_3$[PS$_4$] [1], which already provides relatively good Li$^+$-cation conductivity [7], but not quite as good as when halogenides are introduced as, for example, in Li$_6$PS$_5$*X* (*X* = Cl, Br, I) [4].

The rich structural variety of compounds in the realm of alkali metal-containing *ortho*-thiophosphate realm with rare-earth metal participation, especially within the (A_3[PS$_4$])$_x$ (*RE*[PS$_4$])$_y$ (*A* = alkali metal) system, has been thoroughly addressed already [8]. Those

ortho-thiophosphates(V) are especially known for the heavier alkali metals such as cesium [9–11] potassium [12] or mixed cations like $Cs_2NaRE[PS_4]_2$ [9]. Interestingly, rubidium-containing rare-earth metal thiophosphates contain both $[PS_4]^{3-}$ and $[P_2S_6]^{4-}$ complex anions, for example, in $RbLa[P_2S_6]$ [13], $Rb_3Sm[PS_4]_2$ [10] or $Rb_4Ln[P_2S_6][PS_4]_2$ [14]. On the other hand, when only sodium is used as a monovalent cation, exclusively thiophosphate(IV) groups $[P_2S_6]^{4-}$ are present as complex counter ions [13,15,16]. This seems to be a special case for sodium, as the lightest alkali metal lithium yields compounds with compositions like $Li_9RE_2[PS_4]_5$ ($x = 3$, $y = 2$) [17,18], $Li_6RE_3[PS_4]_5$ ($x = 2$, $y = 3$) [2,18] or $Li_{15}RE_7[PS_4]_{12}$ ($x = 5$, $y = 7$) [19], where again only *ortho*-thiophosphate(V) anions $[PS_4]^{3-}$ are present. Recently, the first thiophosphate with the lightest lanthanoid, namely $Li_3La[PS_4]_2$ ($x = y = 1$) [20], has been published. To synthesize this compound, the lanthanoid trichloride was used as the starting material, though no chlorine was observed in this compound, as confirmed by EDXS measurements. The synthetic route pursued in this paper was similar to the one that led to $Li_3La[PS_4]_2$. However, this time, chlorine did implement itself into the products.

When lanthanum is used as a rare-earth metal, this leads to the formation of orthorhombic $Li_3La[PS_4]_2$ [20]. On the other hand, when Ln = Nd and Sm–Lu are employed, the resulting lithium compounds, either with the phase compositions—$Li_9Ln_2[PS_4]_5$, $Li_6Ln_3[PS_4]_2$ [2,18] or $Li_{15}Ln_7[PS_4]_{12}$ [19]—crystallize in a monoclinic lattice. However, while examining the lighter lanthanoid systems, including chlorine, such as for Ln = Pr, Nd and Sm, crystal formation with an intriguing phenomenon of twinning arises. It appears that the monoclinic structure of the title compounds—$Li_4Ln[PS_4]_2Cl$—mimics a trigonal substructure. Regrettably, no compounds have been discovered so far that incorporate all the elements—lithium, cerium, phosphorus and sulfur at once, so further investigation is required to address this matter. Here, we present the first chloride- and lanthanoid-containing lithium thiophosphates(V) with the structured formula $Li_4Ln[PS_4]_2Cl$ with Ln = Pr, Nd and Sm.

2. Experimental Section

2.1. Solid-State Synthesis

The synthesis of the title compounds—$Li_4Ln[PS_4]_2Cl$ (Ln = Pr, Nd and Sm)—was conducted starting from the lanthanoid trichlorides ($LnCl_3$, Ln = Pr, Nd and Sm: *ChemPur*, Karlsruhe, Germany, 99.9%), phosphorus(V) sulfide (P_2S_5: *Acros Organics*, Geel, Belgium, 98%) and lithium sulfide (Li_2S: *Sigma Aldrich*, Taufkirchen, Germany, 99.9%) in a stoichiometric ratio of 1:1:3, following reaction Equation (1), but originally scheduled to yield the chloride-free thiophosphates $Li_3Ln[PS_4]_2$ in analogy to $Li_3La[PS_4]_2$ [20].

$$RECl_3 + P_2S_5 + 3\,Li_2S \rightarrow Li_4RE[PS_4]_2Cl + 2\,LiCl \tag{1}$$

All substances were handled inside an argon-filled glove box and under strict exclusion of ambient air. The starting materials were placed inside glassy silica ampoules and sealed under a dynamic vacuum. A muffle furnace (*Nabertherm*, Lilienthal, Germany) was programmed to heat the ampoules to 600 °C within 48 h, keep the temperature for 10 h, and then cool gradually back to room temperature over a period of 43 h with 5 h plateaus at 560, 530 and 450 °C.

2.2. Thermal Analysis (DSC)

Differential scanning calorimetric measurements (DSC) were performed on a Netzsch 404 calorimeter. The starting materials—$NdCl_3$, P_2S_5 and Li_2S—were thoroughly ground and filled into a glassy silica ampoule. The temperature program for the measurement was set to ramp from 30 to 800 °C with a rate of 5 °C/min under a constant argon gas flow.

2.3. Single-Crystal X-ray Diffraction (SCXRD)

The synthesis using samarium as lanthanoid yielded crystals sufficient for a single-crystal X-ray diffraction experiment. This measurement was performed on a Bruker-Nonius

κ-CCD diffractometer applying monochromatized Mo-K$_\alpha$ radiation ($\lambda = 71.07$ pm). Through direct-method calculations using SHELXS-97 and refining the calculation via SHELXL-97 [21–23], the crystal structure could be solved first in the trigonal space group $R\overline{3}$ and later in the correct monoclinic space group $C2/c$. Further details on the measurement can be retrieved from FIZ Karlsruhe, 76,344 Eggenstein-Leopoldshafen, Germany (E-mail: crysdata@fiz-karlsruhe.de) under the deposition number CSD 2282010.

2.4. Powder X-ray Diffraction (PXRD)

As only the syntheses with samarium led to single crystals suitable for SCXRD, the isotypic structure of Li$_4$Nd[PS$_4$]$_2$Cl was confirmed by powder X-ray diffractometry. X-ray powder diffraction patterns (PXRD) for the crystal structure refinement were collected on a laboratory powder diffractometer in Debye–Scherrer geometry (Stadi P-diffractometer, *Stoe & Cie*, Darmstadt, Germany, Mo-K$_{\alpha 1}$ radiation from primary Ge(111)-*Johann*-type monochromator, a triple array of Mython 1 K detectors, *Dectris*, Baden, Switzerland). The sample was sealed in a 0.5 mm diameter borosilicate glass capillary (*Hilgenberg glass*, Malsfeld, Germany, no. 0140), which was spun during the measurements, applying a scan time of 16 h.

The program TOPAS 6.0 [24] was used to refine the crystal structure of Li$_4$Nd[PS$_4$]$_2$Cl. Two crystal structure models were extracted from single-crystal XRD data obtained from poor-quality crystals and evaluated using PXRD. The peak profile was described using the fundamental parameter approach of TOPAS [25,26], and the background modeled by *Chebychev* polynomials of 6th order. Both the trigonal and monoclinic cell metrics were evaluated as suitable using *Le Bail* fits [27]. Hence, we performed fully weighted *Rietveld* [28] refinements in order to evaluate both structure models. During the refinements, the thiophosphate-related phosphorus and sulfur positions were constrained using rigid bodies in *z*-matrix notation. Bond lengths and angles were refined, restraining them to reasonable values.

2.5. Energy-Dispersive X-ray Spectroscopy (EDXS)

Several crystals from each reaction were selected, and their elemental composition was determined using an energy-dispersive X-ray spectrometer (*Cameca*, Gennevilliers, France, SX-100, electron microprobe). The samples were placed on a conductive carbon tape (*Plano* G3347, Wetzlar, Germany) and sputtered with carbon to ensure conductive surfaces. The acceleration voltage at which the measurement was conducted was 15.0 keV with a pick-up angle of 40°. The SEM image was taken from the same crystal Li$_4$Sm[PS$_4$]$_2$Cl used for SXRD on the device with the same conditions applied for the EDXS measurements.

2.6. Diffuse Reflectance Spectroscopy (DRS)

To determine the location of the optical band gap of the title compounds, diffuse reflectance spectroscopy was applied. The samples were measured with an integrating sphere at a 45° angle on a *J&M Tidas* (Essingen, Germany) device. The obtained spectra have been analyzed via the *Kubelka—Munk* function [29] to transform reflectance into absorbance.

2.7. Bond-Valence Energy-Landscape (BVEL) Calculations

For the evaluation of possible ion-conducting pathways, theoretical bond-valence energy-landscape calculations were conducted. The program *softBV* (GUI Version 1.0) [30,31] was used for the calculation, and the program VESTA (Version 3.5.7) [32] took care of the visualization.

3. Results and Discussion

3.1. Material and Synthesis

Attempts to synthesize new representatives of the composition of Li$_3$*Ln*[PS$_4$]$_2$ in analogy to the previously published Li$_3$La[PS$_4$]$_2$ [20] following the reaction (2) led to the

new compounds—Li$_4$*Ln*[PS$_4$]$_2$Cl (*Ln* = Pr, Nd and Sm)—with one formally added LiCl equivalent.

$$RECl_3 + P_2S_5 + 3\,Li_2S \rightarrow Li_3RE[PS_4]_2 + 3\,LiCl \tag{2}$$

The oven program used for their synthesis is explained in the experimental section and follows the results obtained from thermoanalytical measurements. It differs slightly from the procedure used to prepare Li$_3$La[PS$_4$]$_2$ in that the reaction temperature was 150 °C less than for the lanthanum compound and ran significantly shorter although having more plateaus.

After the reaction process, single crystals were found and selected for *Ln* = Sm under the argon atmosphere of a glove box, which were solved for their crystal structure using SCXRD data. The structure refinement of Li$_4$Sm[PS$_4$]$_2$Cl served as a starting point for the structure solution of the compounds incorporating *Ln* = Pr and Nd, where no suitable single crystals could be selected. However, powder X-ray diffraction measurements (PXRD) were utilized to confirm whether the structures are isotypic. The refinement of Li$_4$Nd[PS$_4$]$_2$Cl is shown in detail below; however, due to unknown by-products, the refinement could not be accomplished reliably for Li$_4$Pr[PS$_4$]$_2$Cl.

As expected from the stoichiometry of the starting materials and from the experience with the Li$_3$La[PS$_4$]$_2$ [20] synthesis, lithium chloride was found as by-product. Additionally, small amounts of the ternary thiophosphates *Ln*[PS$_4$] and some unidentified by-products could be observed in a few of the powder diffractograms.

To prove the stoichiometric formula resulting from the single-crystal X-ray diffraction experiments to be correct, especially concerning phosphorus, sulfur and chlorine in the compound, EDXS measurements were performed for the samarium-containing single crystal. The results are presented in Table 1 and support the formula of Li$_4$Sm[PS$_4$]$_2$Cl very well. The observed oxygen content may be due to the short time when the sample was not protected by inert-gas conditions during its transfer. The vulnerability of the crystal towards ambient conditions could also be observed in the taken SEM picture (Figure 1), as the surface of the sample looks rather rough. The moisture sensitivity was also confirmed by PXRD measurements. A sample of the bulk material was measured directly after storage under an argon atmosphere and for two consecutive days after being removed from the glove box. The loss of intensity of the reflection over a period of two days stemming from the target compound versus the stable intensities of lithium chloride hinted at a severe degradation of Li$_4$Sm[PS$_4$]$_2$Cl.
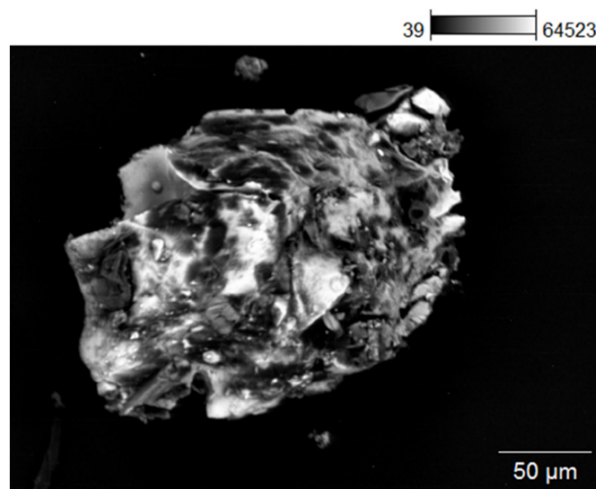

Figure 1. SEM picture of the Li$_4$Sm[PS$_4$]$_2$Cl crystal after the X-ray diffraction experiment. The crystal was exposed for a short time to ambient air.

Table 1. Quantitative results of the EDXS element mapping for $Li_4Sm[PS_4]_2Cl$.

Element, X-ray Absorption Edge	Atom Concentration [%]	Weight Concentration [%]
O, *K*	27.30 ± 0.78	11.75 ± 0.11
P, *K*	11.73 ± 0.34	9.87 ± 0.10
S, *K*	47.19 ± 0.63	41.11 ± 0.18
Cl, *K*	6.51 ± 0.24	6.27 ± 0.08
Sm, *L*	7.37 ± 0.27	30.12 ± 0.37
others	0.16 ± 0.15	0.88 ± 0.26

3.2. Structure Description from Single-Crystal XRD Data and Discussion of PXRD

The title compounds with the structured formula $Li_4Ln[PS_4]_2Cl$ with *Ln* = Pr, Nd and Sm crystallize isotypically in the monoclinic space group type *C*2/*c* with the lattice parameters shown in Tables 2 and 3, allowing twelve formula units in the unit cell. A picture of the extended unit-cell content of $Li_4Sm[PS_4]_2Cl$ as a representative of all three $Li_4Ln[PS_4]_2Cl$ compounds viewed along the *c*-axis and highlighting the complex $[PS_4]^{3-}$ anions is presented in Figure 2.

Table 2. Crystallographic data for the single-crystal measurement of $Li_4Sm[PS_4]_2Cl$ and their determination.

Structured formula	$Li_4Sm[PS_4]_2Cl$	
Molar mass, M_m/g·mol^{-1}	532.05	
Measurement temperature/K	293(2)	
Crystal system	monoclinic	trigonal (substructure)
Space group	*C*2/*c* (no. 15)	$R\bar{3}$ (no. 148)
a/pm	2089.31(12)	1579.67(9)
b/pm	1579.67(9)	1579.67(9)
c/pm	1309.04(8)	2818.36(16)
α/°	90	90
β/°	109.978(3)	90
γ/°	90	120
Number of formula units, *Z*	12	18
Calculated density, D_x/g·cm^{-3}	2.611	2.611
Unit-cell volume, V_{uc}/nm^3	4060.4	6090.6
Molar volume, V_m/cm^3·mol^{-1}	203.76(9)	203.76(9)
Data range, $2\Theta_{max}$/°	55.74	55.76
Index range, $\pm h$, $\pm k$, $\pm l$	21/19/16	20/20/36
F(000)/e$^-$	2988	4482
Absorption coefficient, μ/mm^{-1}	5.96	5.96
BASF *	0.17909	–
Data residuals, R_{int}/$R\sigma$	0.087/0.052	0.248/0.110
Structure residuals, R_1/wR_2	0.057/0.135	0.214/0.423
Goodness of Fit (GooF)	1.056	1.337
Residual electron density (max./min.)/e$^-$·10^6 pm^{-3}	1.03/-1.34	2.71/-4.42
CSD number	2282010	–

* For the monoclinic refinement, the twining law (-0.5 -0.5 1; -0.5 -0.5 -1; 0.5 -0.5 0) was applied.

Table 3. Crystallographic data and Rietveld refinement data of $Li_4Nd[PS_4]_2Cl$.

Structured formula	$Li_4Nd[PS_4]_2Cl$
Molar mass, M_m/g·mol^{-1}	525.963
Measurement temperature/K	295(2)
Crystal system	monoclinic
Space group	*C*2/*c* (no. 15)

Table 3. *Cont.*

a/pm	2098.5(1)
b/pm	1580.6(1)
c/pm	1318.0(1)
$\beta/^\circ$	110.017(5)
Number of formula units, Z	12
Unit-cell volume, V_{uc}/nm^3	4.108(4)
Molar volume, $V_{\text{m}}/\text{cm}^3 \cdot \text{mol}^{-1}$	206.13(6)
Calculated density, $\rho_{\text{calc}}/\text{g} \cdot \text{cm}^{-3}$	2.552
Wavelength/pm	70.93
R-p/% *	3.83
R-wp/% *	5.42
R-F^2/% *	2.08
Starting angle ($^\circ$, 2θ)	0
Final angle ($^\circ$, 2θ)	110
Step width ($^\circ$, 2θ)	0.01
Time/scan (h)	16
Number of variables	94
CSD number	2,282,748

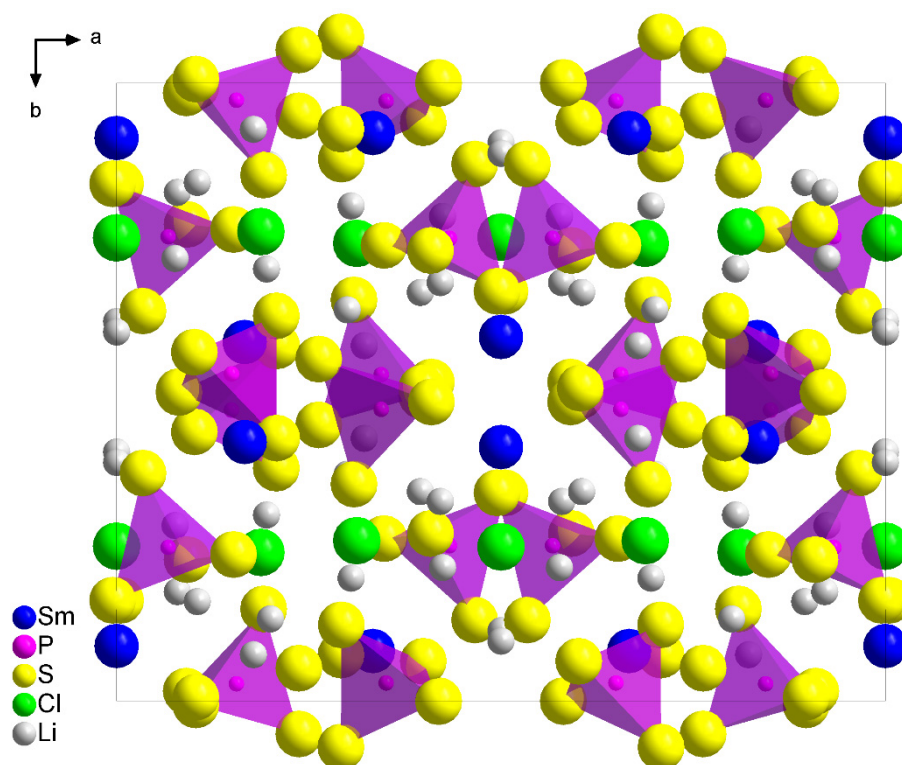* R-p, R-wp and R-F^2 as defined in TOPAS (Bruker AXS) [24].

Figure 2. Extended unit-cell content of $Li_4Sm[PS_4]_2Cl$ with highlighted $[PS_4]^{3-}$ tetrahedra as viewed along the *c*-axis.

The single-crystal structure refinement could only be solved satisfyingly by introducing the two-fold twinning law (−0.5 −0.5 1; −0.5 −0.5 −1; 0.5 −0.5 0) into the calculation. Without this implementation, the structure solution appears to be also possible using the trigonal space group $R\bar{3}$, due to generating symmetry on all three axes. The calculated solution in $R\bar{3}$ seemed chemically very plausible; however, the weighted R_2-value was far too high (w$R_2 \approx 0.43$), as well as other refinement values (Table 2). This supported the solution in the monoclinic space group $C2/c$, which led to the data presented in this article with the quality indices shown in Table 2. The concept of the trigonal lattice, as well as an explanation for the tendency of crystals to form twins, becomes clear when observing

the $2 \times 2 \times 2$ unit cell from the viewing direction of $[1\,0\,\bar{1}]$. The threefold axis through all chloride anions suggests trigonal symmetry (Figure 3).
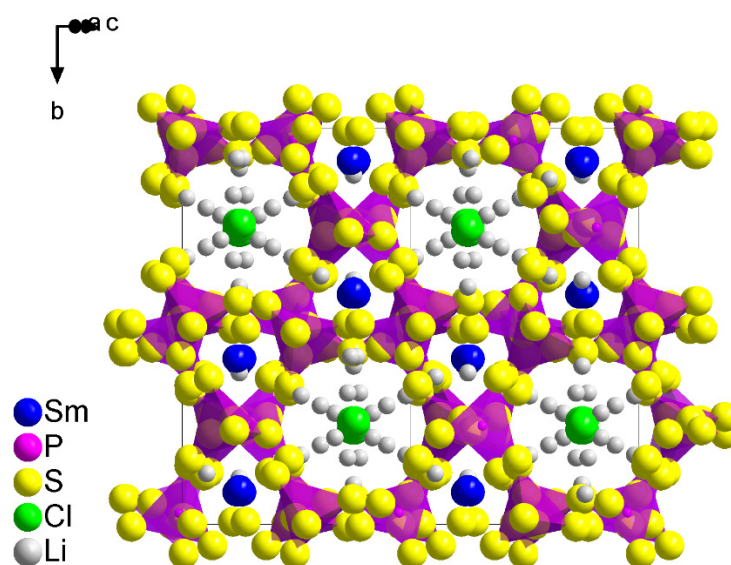

Figure 3. Extended unit-cell content of $Li_4Sm[PS_4]_2Cl$ with highlighted $[PS_4]^{3-}$ tetrahedra as viewed along $[1\,0\,-1]$ to visualize the putative trigonal symmetry leading to twinning.

The graphical results of the PXRD refinements for the neodymium-containing phase are presented in Figure 4 for the trigonal setting and Figure 5 for the monoclinic one. Both structure models led to acceptable residuals (trigonal structure: $R = 6.28\%$, monoclinic structure: $R = 5.42\%$). The graphical result of the fit using the monoclinic structure model is clearly better than the fit for the trigonal one, in particular in the range between $2\theta° = 10$ and $20°$. Although this is partially attributed to the increased number of parameters used for the refinement (monoclinic model: 94 independent parameters, trigonal model: 75 independent parameters), we evaluate the monoclinic structure model as more suitable. We suggest that the monoclinic structure refinement as a superstructure reflects the actual crystal structure of $Li_4RE[PS_4]_2Cl$ better than the trigonal setting. The crystallographic data are given in Table 3.

The PXRD pattern of $Li_4Pr[PS_4]_2Cl$ shows vast similarities to the neodymium analog; hence, we expected this phase to crystallize in the same monoclinic structure. A close inspection of the diffraction data revealed the presence of LiCl (Figure 6, green tick marks) and of unindexed reflections (Figure 6, grey line, e.g., at $2\theta° = 7.5$, 13.5 and $13.7°$). As the diffractogram cannot be indexed, including these reflections, and as a symmetry reduction or using a reasonable supercell, does not lead to a proper description of these peaks, we assigned them to an unidentified by-product. Due to peak overlaps, we were not able to perform a fully weighted Rietveld [28] refinement of $Li_4Pr[PS_4]_2Cl$, so we extracted the lattice parameters from a Le Bail fit [27]. Thus, $Li_4Pr[PS_4]_2Cl$ crystallizes in the space group $C2/c$ with $a = 2104.5(6)$ pm, $b = 1581.3(3)$ pm, $c = 1322.3(5)$ pm and $\beta = 110.02(3)°$ for $Z = 12$ (Table 4). These axes would correspond to $a = 1581$ pm, $b = 1590$ pm and $c = 2842$ pm, if the structure were set up trigonally. The a- and b-axis differ slightly as these values are recalculated from the monoclinic results, showing once more that the monoclinic version is indeed more precise. The exact peak positions and integral peak intensities of the unknown by-product were extracted by single line fits (Table 5). These peaks do not match any reference data of known lithium or praseodymium chlorides, thiophosphates, phosphates or mixed chloride thiophosphate phases.
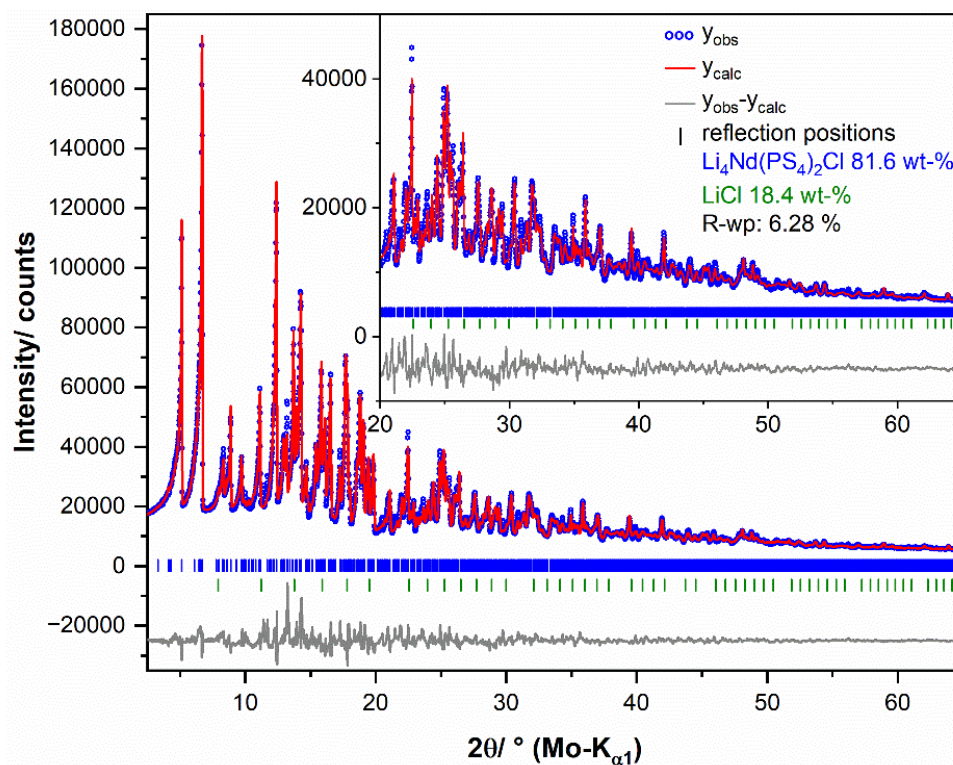
Figure 4. Graphical result of the final Rietveld refinement of $Li_4Nd[PS_4]_2Cl$ using the trigonal structure model with space group $R\overline{3}$ and a = 1584.09(8) pm, c = 2834.49(15) pm for Z = 18. The high-angle part starting at 2Θ = 20° is enlarged for clarity.
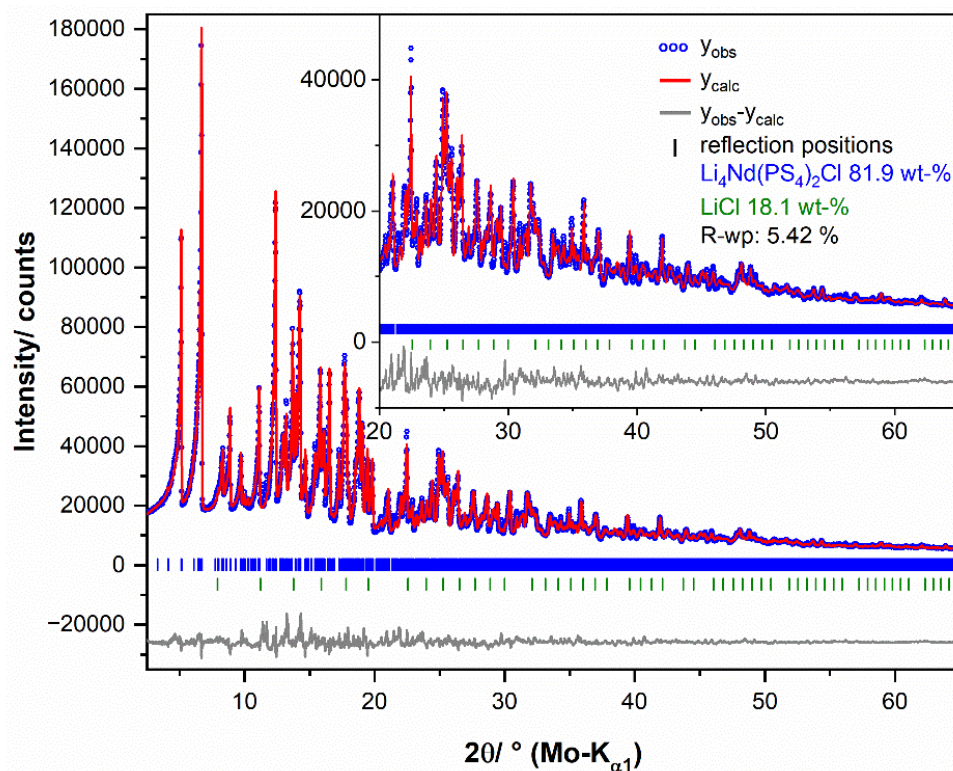

Figure 5. Graphical result of the final Rietveld refinement of $Li_4Nd[PS_4]_2Cl$ using the monoclinic structure model with space group $C2/c$ and a = 2098.54(11) pm, b = 1580.60(8) pm, c = 1318.02(9) pm, β = 110.018(4)° for Z = 12. The high-angle part starting at 2Θ = 20° is enlarged for clarity.

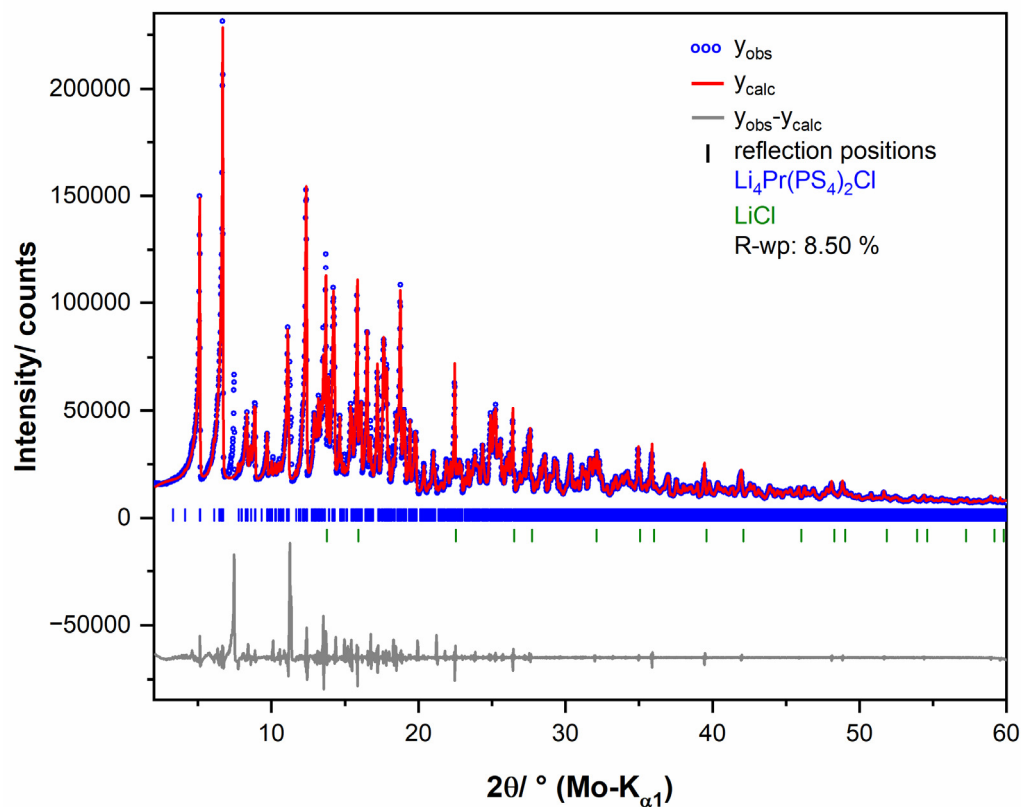**Figure 6.** Graphical result of the final Le Bail fit [27] for $Li_4Pr[PS_4]_2Cl$.

Table 4. Crystallographic data of $Li_4Pr[PS_4]_2Cl$.

Structured formula	$Li_4Pr[PS_4]_2Cl$
Molar mass, Mm/g·mol^{-1}	525.963
Measurement temperature/K	295(2)
Crystal system	monoclinic
Space group	$C2/c$ (no. 15)
a/pm	2104.5(6)
b/pm	1581.3(3)
c/pm	1322.3(5)
β/°	110.02(3)
Number of formula units, Z	12
Unit-cell volume, V_{uc}/nm^3	4.134(3)
R-wp/%	0.085

Table 5. List of peak positions and integral peak intensities of the unidentified by-product in the $Li_4Pr[PS_4]_2Cl$ sample.

Peak Number	Peak Position	d/pm	Relative Integral Peak Intensity
1	7.468	544.5	41.0
2	8.414	483.5	8.6
3	10.112	402.4	12.7
4	10.571	385.0	10.4
5	10.865	374.6	4.0
6	10.925	372.6	5.7
7	11.257	361.6	75.1
8	11.345	358.8	49.2
9	13.126	310.3	22.7
10	13.433	303.2	19.8

Table 5. *Cont.*

Peak Number	Peak Position	*d*/pm	Relative Integral Peak Intensity
11	13.522	301.2	100.0
12	13.715	297.0	96.8
13	14.376	283.4	37.2
14	14.966	272.3	31.6
15	15.187	268.4	15.1
16	15.241	267.4	13.5
17	15.435	264.1	43.4
18	16.747	243.5	71.9
19	16.973	240.3	10.5
20	17.184	237.4	71.6
21	17.368	234.9	0.9
22	18.304	223.0	50.5
23	18.468	221.0	64.6
24	19.948	204.8	42.0
25	21.227	192.6	58.6
26	21.799	187.6	16.3

In total, there are 27 different crystallographic sites within the monoclinic structure presented in Table 6 for the single-crystal X-ray diffraction experiment of $Li_4Sm[PS_4]_2Cl$. For comparison, the 19 crystallographic sites of the trigonal representation are depicted in Table 7. The crystallographic coordinates for $Li_4Nd[PS_4]_2Cl$ from the powder X-ray diffraction experiments are shown in Table 8.

There are two crystallographically different samarium sites. Both Sm1 and Sm2 are coordinated by eight sulfur atoms in the shape of bicapped trigonal prisms, with distances as presented in Table 9.

This appears quite usual for lanthanoids; however, it is slightly different than in the ternary thiophosphates $Ln[PS_4]$ [33] or in $Li_3La[PS_4]_2$ [20], where the eightfold coordinated Ln^{3+} cations are centering trigonal dodecahedra. The bond lengths are within the usual range of $[LnS_8]^{13-}$ polyhedra with d(Sm–S) = 280–299 pm comparing well with those in $Sm[PS_4]$ (285–294 pm) [33]. The coordination polyhedron around Sm2 is slightly more distorted than the one for Sm1. These bicapped trigonal prisms of sulfur are constructed by $[PS_4]^{3-}$ tetrahedra, whose ligands surround the three different phosphorus sites. The P–S distances are very much in the usual range for the complex $[PS_4]^{3-}$ anions with bond lengths between 200 and 207 pm along with "tetrahedral" angles ranging from 106 to 112°.

Table 6. Atomic coordinates and equivalent isotropic displacement parameters for $Li_4Sm[PS_4]_2Cl$ (monoclinic, $C2/c$).

Atom	*Wyckoff* Site	*x*/*a*	*y*/*b*	*z*/*c*	U_{eq} */pm^2
Sm1	4*e*	$1/2$	0.41098 (8)	$1/4$	0.0201 (4)
Sm2	8*f*	0.33338 (5)	0.08096 (6)	0.42856 (6)	0.0186 (3)
P1	8*f*	0.1558 (3)	0.0280 (3)	0.3298 (3)	0.0198 (11)
P2	8*f*	0.4330 (3)	0.2513 (3)	0.3808 (3)	0.0204 (11)
P3	8*f*	0.1494 (3)	0.4707 (3)	0.2997 (3)	0.0205 (12)
Cl1	4*e*	0	0.2506 (6)	$1/4$	0.076 (3)
Cl2	8*f*	0.1877 (3)	0.2405 (4)	0.0696 (3)	0.0413 (14)
S1	8*f*	0.3969 (3)	0.4938 (3)	0.3252 (3)	0.0284 (13)
S2	8*f*	0.0906 (3)	0.0161 (3)	0.4135 (3)	0.0277 (13)
S3	8*f*	0.1912 (3)	0.1490 (3)	0.3394 (3)	0.0243 (12)
S4	8*f*	0.2629 (3)	0.4468 (3)	0.1049 (3)	0.0287 (12)
S5	8*f*	0.4657 (3)	0.1312 (3)	0.4187 (3)	0.0297 (13)
S6	8*f*	0.4948 (2)	0.3369 (3)	0.0384 (3)	0.0236 (11)

Table 6. *Cont.*

Atom	*Wyckoff* Site	x/a	y/b	z/c	U_{eq} */pm^2
S7	8f	0.4083 (3)	0.2711 (3)	0.2176 (3)	0.0333 (15)
S8	8f	0.3479 (3)	0.2629 (3)	0.4239 (3)	0.0252 (12)
S9	8f	0.2077 (3)	0.3768 (3)	0.3852 (3)	0.0338 (14)
S10	8f	0.1011 (3)	0.4356 (3)	0.1436 (3)	0.0255 (12)
S11	8f	0.2918 (3)	0.0745 (3)	0.2011 (3)	0.0281 (13)
S12	8f	0.4188 (3)	0.0008 (3)	0.1243 (3)	0.0266 (13)
Li1	4e	0	0.403 (3)	$^1/_4$	0.048 (13)
Li2	4e	$^1/_2$	0.114 (3)	$^1/_4$	0.056 (14)
Li3 [†]	8f	0.076 (7)	0.284 (7)	0.079 (8)	0.11 (4)
Li4 [†]	8f	0.105 (7)	0.161 (8)	0.132 (9)	0.12 (4)
Li5	8f	0.305 (2)	0.199 (3)	0.093 (3)	0.063 (11)
Li6	8f	0.079 (2)	0.177 (3)	0.401 (3)	0.068 (11)
Li7	8f	0.178 (3)	0.075 (4)	0.064 (5)	0.12 (2)
Li8	8f	0.300 (5)	0.367 (5)	0.329 (6)	0.13 (2)

* $^1/_3[U_{22} + 1/\sin^2\beta\,(U_{11} + U_{33} + 2U_{13}\cos\beta)]$ [34], [†] fixed site occupancy of $^1/_2$.

Table 7. Atomic coordinates and equivalent isotropic displacement parameters for $Li_4Sm[PS_4]_2Cl$ (trigonal, $R\bar{3}$).

Atom	*Wyckoff* Site	x/a	y/b	z/c	U_{eq} */pm^2
Sm	18f	0.33662 (18)	0.33405 (17)	0.08330 (8)	0.0309 (7)
P1	18f	0.3743 (7)	0.1807 (6)	0.0036 (3)	0.0204 (19)
P2	18f	0.5131 (7)	0.0391 (8)	0.1629 (3)	0.023 (2)
Cl1	6c	0	0	0.0689 (6)	0.028 (3)
Cl2	6c	0	0	0.2447 (6)	0.045 (5)
Cl3	6c	0	0	0.4374 (5)	0.038 (4)
S1	18f	0.3287 (7)	0.4771 (7)	0.0168 (3)	0.026 (2)
S2	18f	0.0951 (10)	0.4181 (10)	0.0075 (4)	0.043 (3)
S3	18f	0.3496 (7)	0.1588 (7)	0.0746 (4)	0.026 (2)
S4	18f	0.1578 (8)	0.2475 (9)	0.0322 (5)	0.049 (4)
S5	18f	0.0117 (8)	0.2500 (12)	0.1593 (4)	0.045 (3)
S6	18f	0.1854 (6)	0.1897 (7)	0.1503 (3)	0.0231 (19)
S7	18f	0.2406 (12)	0.4196 (10)	0.1340 (6)	0.056 (4)
S8	18f	0.4929 (7)	0.0140 (7)	0.0911 (3)	0.024 (2)
Li1	18f	0.515 (4)	0.186 (4)	0.091 (2)	0.016 (11)
Li2	18f	0.165 (6)	0.023 (6)	0.065 (3)	0.036 (17)
Li3	18f	0.030 (4)	0.334 (4)	0.0916 (17)	0.008 (9)
Li4	18f	0.171 (5)	0.550 (5)	0.067 (3)	0.032 (15)

* $^1/_3[U_{33} + \,^4/_3\,(U_{11} + U_{22} - U_{12})]$ [34].

Table 8. Atomic coordinates of monoclinic $Li_4Nd[PS_4]_2Cl$ stemming from the powder X-ray diffraction data.

Atom	*Wyckoff* Site	x/a	y/b	z/c
Nd1	4e	$^1/_2$	0.4146 (8)	$^1/_4$
Nd2	8f	0.3342 (4)	0.0813 (1)	0.4287 (6)
P1	8f	0.1587 (19)	0.024 (2)	0.339 (2)
P2	8f	0.4365 (17)	0.255 (3)	0.393 (3)
P3	8f	0.15663 (18)	0.481 (2)	0.310 (3)
Cl1	4e	0	0.229 (2)	$^1/_4$
Cl2	8f	0.1833 (12)	0.245 (2)	0.055 (2)
S1	8f	0.200 (7)	0.149 (5)	0.345 (9)
S2	8f	0.112 (5)	0.015 (7)	0.184 (4)

Table 8. *Cont.*

Atom	*Wyckoff* Site	*x/a*	*y/b*	*z/c*
S3	8*f*	0.096 (4)	0.014 (6)	0.424 (6)
S4	8*f*	0.263 (3)	0.430 (5)	0.103 (7)
S5	8*f*	0.497 (4)	0.339 (6)	0.028 (5)
S6	8*f*	0.360 (3)	0.266 (6)	0.445 (5)
S7	8*f*	0.415 (6)	0.278 (6)	0.224 (5)
S8	8*f*	0.471 (4)	0.127 (4)	0.430 (6)
S9	8*f*	0.119 (5)	0.440 (7)	0.162 (4)
S10	8*f*	0.296 (5)	0.088 (5)	0.200 (7)
S11	8*f*	0.220 (5)	0.380 (6)	0.400 (6)
S12	8*f*	0.412 (4)	0.017 (7)	0.125 (7)
Li1	4*e*	0	0.402	$1/4$
Li2	4*e*	$1/2$	0.120	$1/4$
Li3 [†]	8*f*	0.079	0.275	0.097
Li4 [†]	8*f*	0.104	0.168	0.120
Li5	8*f*	0.303	0.198	0.094
Li6	8*f*	0.076	0.176	0.403
Li7	8*f*	0.174	0.078	0.071
Li8	8*f*	0.306	0.382	0.321

[†] fixed site occupancy of $1/2$.

Table 9. Selected interatomic distances (d/pm) for $Li_4Sm[PS_4]_2Cl$ (monoclinic, $C2/c$). For further details on the remaining distances as well as the angles between the atoms, see the entries in the ICSD.

Atoms	*d*/pm	Atoms	*d*/pm
Sm1–S2	285.5 (4)	Sm2–S11	280.4 (4)
Sm1–S2	285.5 (4)	Sm2–S4	285.1 (5)
Sm1–S7	286.0 (5)	Sm2–S12	288.0 (4)
Sm1–S7	286.0 (5)	Sm2–S8	289.3 (5)
Sm1–S1	296.1 (5)	Sm2–S5	292.0 (6)
Sm1–S1	296.1 (5)	Sm2–S9	292.5 (5)
Sm1–S6	297.5 (4)	Sm2–S10	298.7 (5)
Sm1–S6	297.5 (4)	Sm2–S3	299.5 (5)
P1–S1	202.3 (5)	P2–S5	201.9 (6)
P1–S2	202.7 (7)	P2–S6	203.3 (6)
P1–S3	203.8 (6)	P2–S7	204.3 (5)
P1–S4	206.8 (7)	P2–S8	205.0 (7)
P3–S9	200.2 (6)		
P3–S10	202.3 (5)		
P3–S11	205.0 (7)		
P3–S12	205.2 (7)		
Cl1–Li6	239 (4)	Cl2–Li5	240 (4)
Cl1–Li6	239 (4)	Cl2–Li5	244 (5)
Cl1–Li1	241 (5)	Cl2–Li3	248 (13)
		Cl2–Li4	249 (14)
		Cl2–Li7	262 (6)

In the trigonal setting, there is only one Sm^{3+} site present, as expected, also coordinated by eight sulfur atoms with d(Sm–S) = 284–300 pm, which belong to only two crystallographically distinct $[PS_4]^{3-}$ tetrahedra. The three resulting samarium surroundings, two from the monoclinic refinement and one from the trigonal one, are depicted in Figure 7 for comparison, but all show the edge-grafting of four $[PS_4]^{3-}$ units at the Sm^{3+} centers.
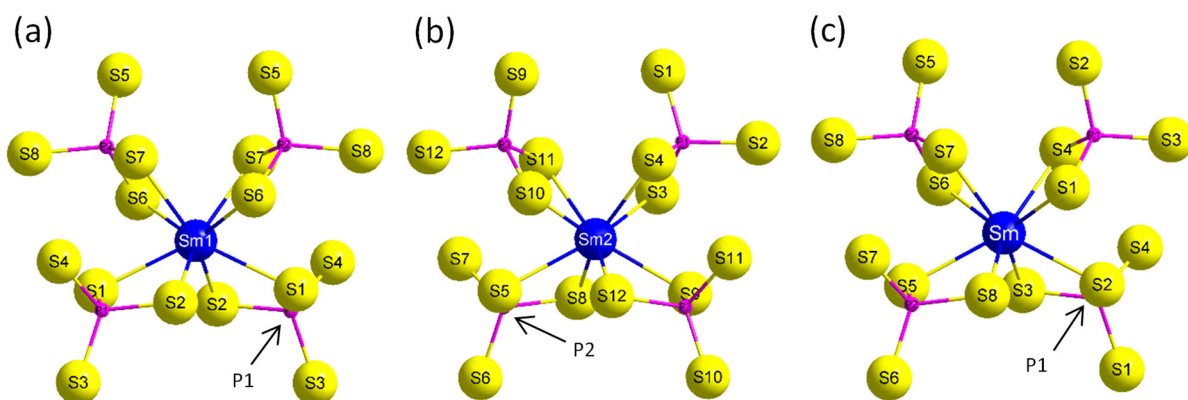
Figure 7. Coordination environments for the Sm^{3+}-cation sites in the monoclinic structure refinement of $Li_4Sm[PS_4]_2Cl$ (Sm1, (**a**); Sm2, (**b**) and for the trigonal refinement for the single Sm^{3+} site, (**c**).

In the monoclinic structure solution, the $[(Sm2)S_8]^{13-}$ polyhedra, linked via $[(P3)S_4]^{3-}$ anions, developed infinite strands along the *c*-axis. These strands are connected via $[(P1)S_4]^{3-}$, $[(Sm1)S_8]^{13-}$ and $[(P2)S_4]^{3-}$ polyhedra along [110], forming the three-dimensional network $^3_\infty\left\{(Sm[PS_4]_2)^{3-}\right\}$ (Figure 8) of the $Li_4Sm[PS_4]_2Cl$ structure.
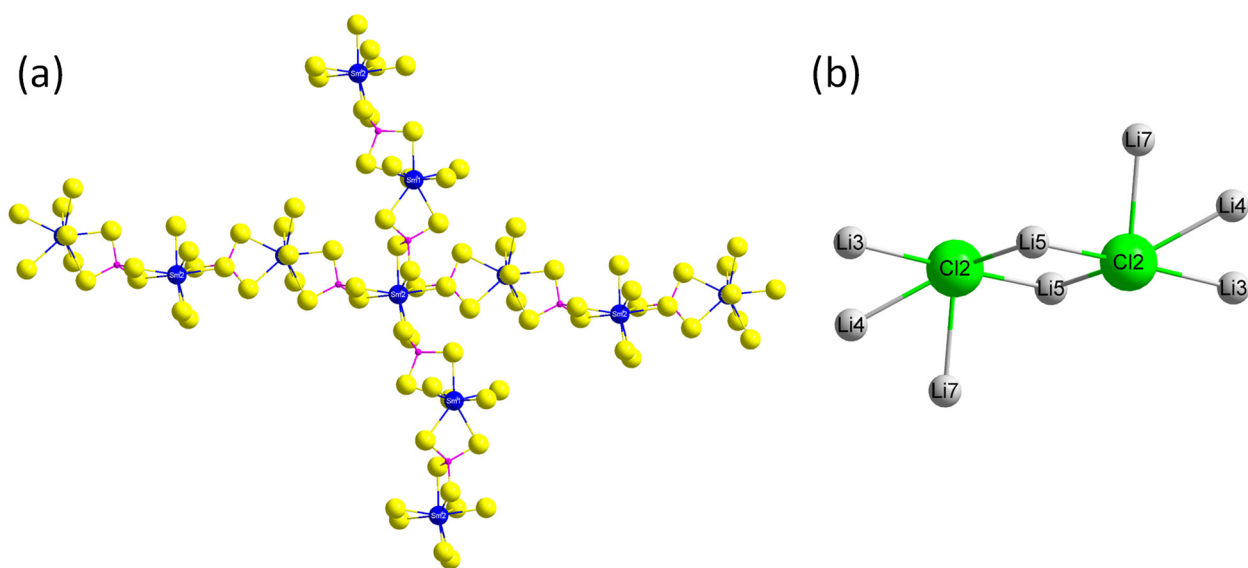
Figure 8. (**a**) $[PS_4]^{3-}$-connected network of $[SmS_8]^{13-}$ polyhedra in both structure descriptions of $Li_4Sm[PS_4]_2Cl$ and (**b**) dimers of $(Cl2)^-$-centered $(Li^+)_5$ square pyramids sharing an edge.

Moreover, there are two different chlorine sites, with Cl1 having three lithium atoms in closer proximity ($d((Cl1)–Li) = 239–241$ pm) and Cl2 with five of them. However, around $(Cl2)^-$, one of the Li^+ cations is further away; thus, describing the coordination sphere as a 4 + 1 environment might seem more plausible. The distances between $(Cl2)^-$ and Li^+ are $d((Cl2)–Li) = 240–249$ pm *plus* 261 pm). The $(Cl2)^-$ anions form interesting dimers (Figure 8), where it almost seems like the Li^+ cations meander around the two chloride anions. The Cl^- anions are bridged by two $(Li5)^+$ cations and end in three terminal lithium ions on either side. Finally, the $(Cl1)^-$ anions separate these dimers from each other.

The chlorine positions themselves, however, are quite interesting as they appear to be residing within channel-like pores made of $[PS_4]^{3-}$ tetrahedra, quite similar to the $Li_6[PS_4]SCl$ [6] case. These channels can best be seen when viewing the monoclinic unit cell along [1 0 −1] direction (Figure 3).

There are eight crystallographically distinct Li^+-cation positions within the crystal structure of $Li_4Sm[PS_4]_2Cl$. $(Li1)^+$, which is surrounded by four sulfur atoms and one Cl^- anion, as well as $(Li6)^+$ and $(Li7)^+$; however, the shape of the $[LiS_4Cl]^{8-}$ polyhedra differ strongly from each other. Two of the bonds from $(Li1)^+$ to S^{2-} are rather long (295 pm), and the coordination polyhedron can therefore be described as $[(Li1)S_{2+2}Cl]^{8-}$. This is not the case for $(Li6)^+$, where there are also longer bonds (292 and 276 pm), but there is no clear cutoff as there is for $(Li1)^+$. The shape of the polyhedron surrounding $(Li7)^+$ is more closely related to the $(Li6)^+$-centered polyhedron, but now the angles are slightly different. The distances between the central lithium and the adjacent sulfur range from 244 to 289 pm. For all three lithium cations, $(Li1)^+$, $(Li6)^+$ and $(Li7)^+$, the distances to the chloride ligand range between 236 and 260 pm. The coordination surrounding $(Li2)^+$ is rather unique as there are six sulfur atoms surrounding it in the shape of a heavily distorted octahedron. However, there are four shorter distances (256–262 pm) and two much longer ones (2×307 pm). On the other hand, $(Li8)^+$ is coordinated by four sulfur atoms, though strongly distorted, so it somehow bridges the relation between $(Li2)^+$ and $(Li6)^+$ as it does not show the two extra sulfur ligands at rational distances and the four coordinating sulfur atoms are 210–304 pm apart. Two chlorine and two sulfur ligands coordinate the $(Li5)^+$ cation in the shape of a distorted tetrahedron. The bond lengths between lithium and chlorine range from 238 to 245 pm, and the distance between the $(Li5)^+$ and sulfur is 249 pm. $(Li3)^+$ is coordinated by one chlorine and three sulfur ligands. This $[LiS_3Cl]^{6-}$ polyhedron is a motif also present for $(Li4)^+$. The shape of these coordination environments is a chair-like geometry showing for both $(Li3)^+$ and $(Li4)^+$, very similar with distances ranging from 247 to 286 pm with the Li–Cl bond being the shortest one in the case of $(Li3)^+$.

Only four crystallographically distinct sites in the trigonal refinement host Li^+ cations achieve charge neutrality (Table 8). If some of them might suffer from only partial occupation, two more show up in the difference *Fourier* map of the final refinement. Both refer to the special positions $9e$ ($^1/_2$, 0, 0) and $9f$ ($^1/_2$, 0, $^1/_2$), which could represent pseudo-octahedral migration pathway stops with six distances from lithium to the involved sulfur atoms between 243 and 258 pm for each one of them. Attempts for their inclusion in the structure refinements did not reduce the residuals and resulted in unstable values for their calculated occupation factors and U_{eq} parameters. Since locating lithium atoms from X-ray diffraction experiments is already challenging, there remains, of course, no physical evidence to support this claim. However, it further strengthens the argumentation for the monoclinic description being more feasible.

3.3. Diffuse Reflectance Spectroscopy

To determine the location of the optical band gap of the three title compounds—Li_4 *Ln*$[PS_4]_2Cl$ (*Ln* = Pr, Nd and Sm)—diffuse reflectance spectroscopy was applied, and Figures 9–11 show the obtained plots. The band gap can be read off as the x-value at the intersection of the tangents before and after the step. However, one has to keep in mind that there are by-products present that potentially change the location of the band gaps slightly. The band gaps for the three bulk products are $E_g = 3.49$ eV ($\widehat{=} \lambda = 355$ nm) for the mint green praseodymium, $E_g = 3.52$ eV ($\widehat{=} \lambda = 352$ nm) for the pastel blue neodymium and $E_g = 2.69$ eV ($\widehat{=} \lambda = 461$ nm) for the yellow samarium compound. Also, within these spectra, sharp and characteristic $f \rightarrow f$ transitions are visible. They can be attributed using the *Dieke* diagram [35] and correspond well to the ones of the respective *f*-element trication Ln^{3+}.
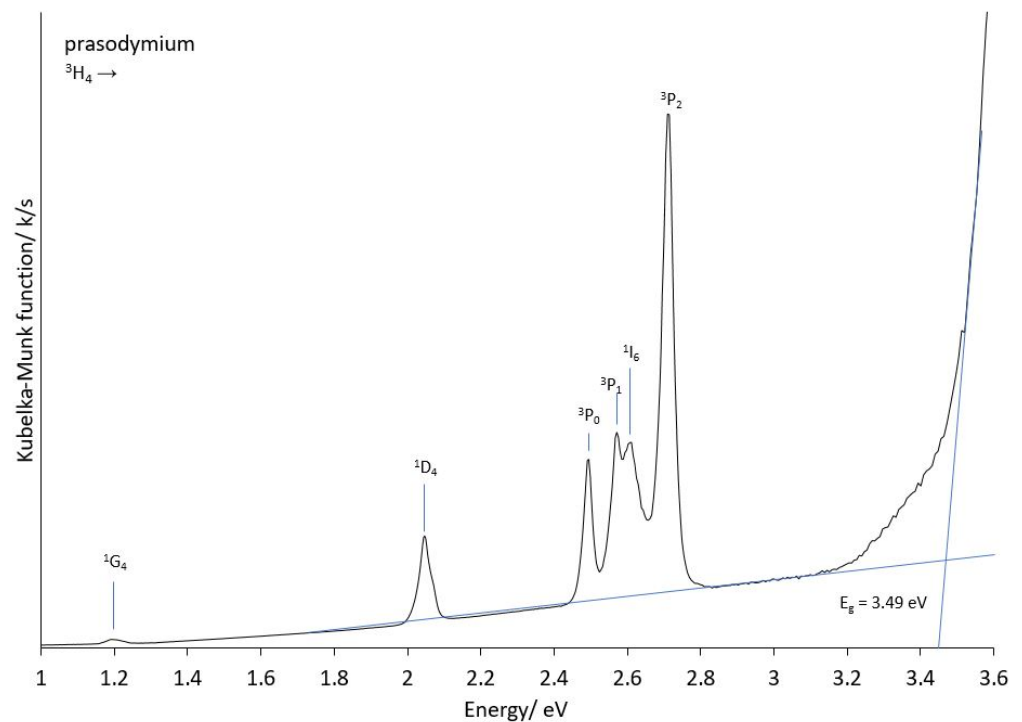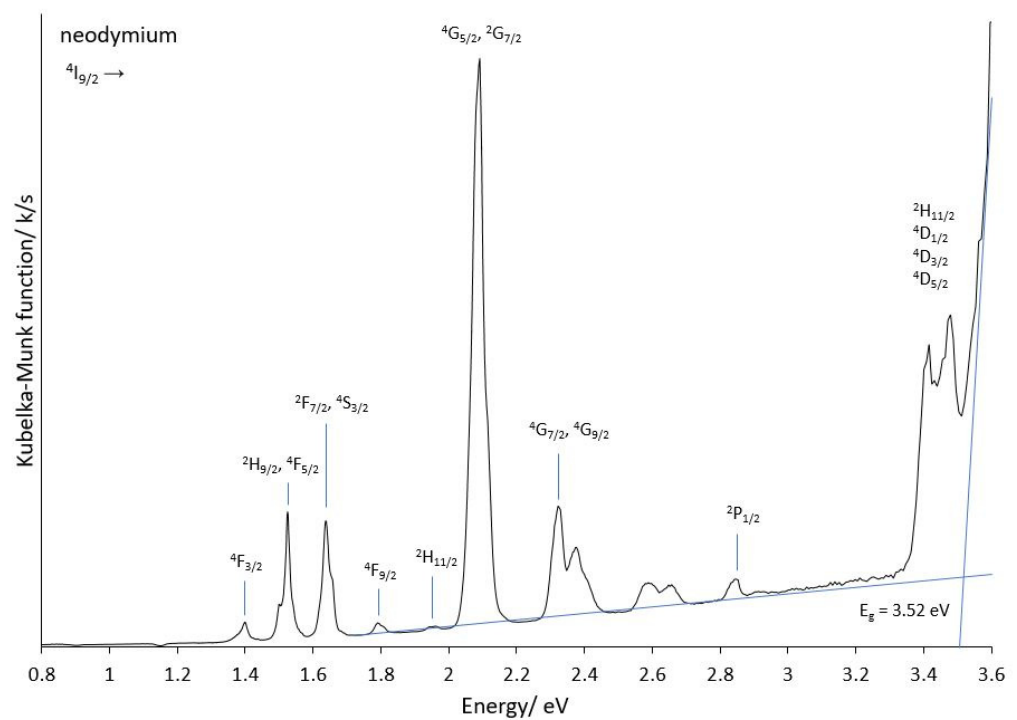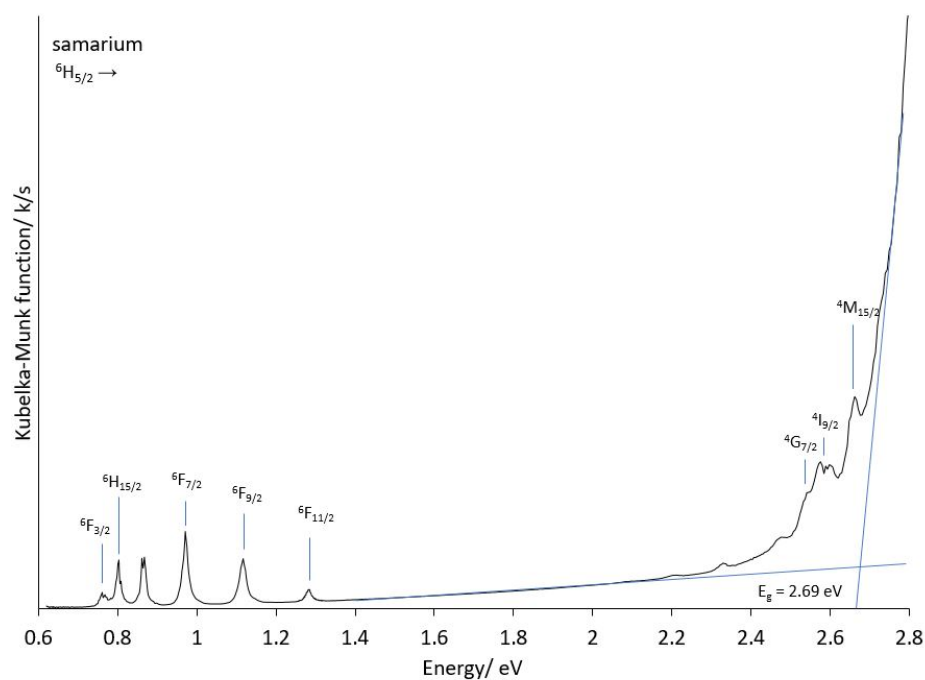
Figure 9. *Kubelka—Munk* plot from DRS data to determine the optical band gap to be 3.49 eV with assigned $f \rightarrow f$ transitions for the bulk praseodymium material $Li_4Pr[PS_4]_2Cl$.

Figure 10. *Kubelka—Munk* plot from DRS data to determine the optical band gap to be 3.52 eV with assigned $f \rightarrow f$ transitions for the bulk neodymium material $Li_4Nd[PS_4]_2Cl$.

Figure 11. *Kubelka—Munk* plot from DRS data to determine the optical band gap to be 2.69 eV with assigned $f \to f$ transitions for the bulk samarium material $Li_4Sm[PS_4]_2Cl$.

3.4. Bond-Valence Energy-Landscape (BVEL) Calculations

The bond-valence energy landscapes were calculated as stated in the experimental section in order to find the most probable diffusion pathways of the Li^+ cations within the crystal structure model of $Li_4Sm[PS_4]_2Cl$, as obtained from the SCXRD experiments, giving a glimpse at the potential performance of the material as an ion conductor. The diffusion pathways can be plotted as isosurfaces at different levels using VESTA [32] (Figure 12).
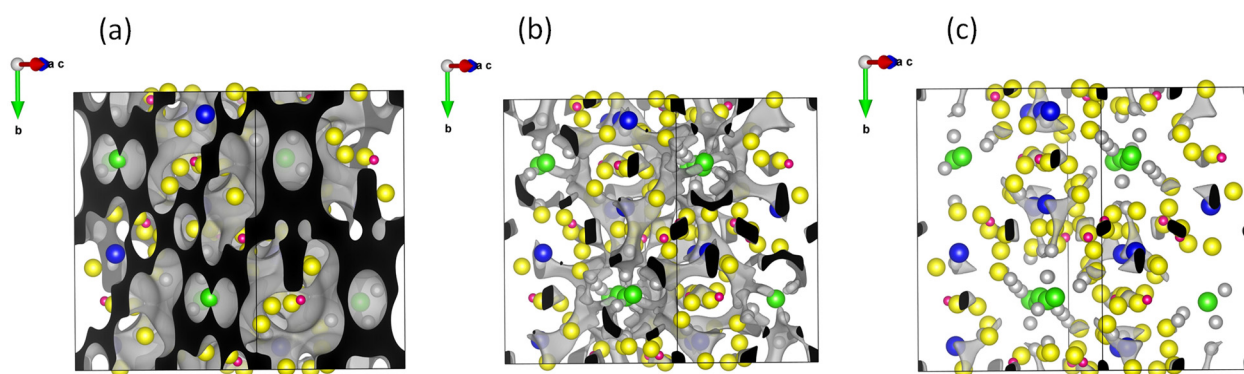
Figure 12. Bond-valence energy-landscape isosurfaces with different depth levels for $Li_4Sm[PS_4]_2Cl$ (monoclinic, $C2/c$) with levels 0.3 (**a**), 1.9 (**b**) and 2.3 (**c**).

The calculated activation energies for the one-dimensional pathways for the Li^+-cation mobility is $E_a(Li^+) = 0.88$ eV. This appears to be quite high, though reasonable, keeping in mind that the lithium cations are mostly bound to the chloride anions sitting in what can be described as tunnels in the structure. In other lithium-containing rare-earth metal thiophosphates(V), for example, $Li_3La[PS_4]_2$ (1D-$E_a(Li^+) = 0.44$ eV) [20] or $Li_9Ho_2[PS_4]_5$ (1D-$E_a(Li^+) = 0.38$ eV) [19], the energy barrier is lower than the chloride-containing one, as expected, due to only one sort of anion being present. The bond-valence energy landscapes give a direction on what could be the diffusion behavior of the ions, but experimental data

are crucial. So, taking a look at the ionic conductivity of these materials has to be carried out in the next step once phase pure samples are available.

4. Conclusions

The synthesis of three new compounds with the structured formula Li$_4$*Ln*[PS$_4$]$_2$Cl (*Ln* = Pr, Nd and Sm) was performed through reactions of *Ln*Cl$_3$, P$_2$S$_5$ and Li$_2$S. Single crystals were obtained only for the samarium compound, and the crystal structure was determined using SCXRD. EDXS measurements supported the stoichiometric formula of Li$_4$Sm[PS$_4$]$_2$Cl. For *Ln* = Nd and Pr, powder X-ray diffraction measurements confirmed the isotypic nature of all three compounds. Expected by-products, including LiCl and *RE*[PS$_4$] as expected, however, were observed in the bulk samples, impeding the exact analysis of the praseodymium representative. The compounds crystallize in the monoclinic space group *C*2/*c*. A threefold axis through the chloride anions is indicated in the crystal structure. Thus, a trigonal substructure is observed, but both SCXRD and PXRD refinements suggest the monoclinic structure model is more suitable than the trigonal one. Both Sm^{3+}-cation sites are coordinated by eight sulfur atoms in a bicapped trigonal prismatic configuration, while three distinct [PS$_4$]$^{3-}$ tetrahedra result from the twelve sulfur atoms surrounding the three different phosphorus sites. The compounds form a three-dimensional network through the connection of [(Sm2)S$_8$]$^{13-}$- and [(P3)S$_4$]$^{3-}$-containing strands cross-linked via [(P1)S$_4$]$^{3-}$, [(Sm1)S$_8$]$^{13-}$ and [(P2)S$_4$]$^{3-}$ units. Two distinct chloride sites exhibit interesting dimeric arrangements involving the bridging Li$^+$ cations. The latter shows irregular coordination figures varying from six sulfur atoms to a mixture of two chlorides and two sulfur ligands.

In conclusion, the structure solution of the new Li$_4$*Ln*[PS$_4$]$_2$Cl compounds could be successfully performed with single-crystal X-ray diffraction data obtained for *Ln* = Sm, and isotypic behavior was confirmed for *Ln* = Nd and Pr by PXRD. All compounds crystallize monoclinically in the space group *C*2/*c* with apparent channel-like features in the structure, thus hinting at possible diffusion pathways for both Li$^+$ and Cl$^-$ ions. BVEL calculations were performed, but further investigations and analyses are required to explore the properties and potential applications of these newly synthesized materials.

References

1. Mercier, R.; Malugani, J.-P.; Fahys, B.; Robert, G.; Douglade, J. Structure du tetrathiophosphate de lithium. *Acta Crystallogr.* **1982**, *B38*, 1887–1890. [CrossRef]
2. Müller, C.; Jörgens, S.; Mewis, A. Neue Thiophosphate: Die Verbindungen Li$_6$*Ln*$_3$(PS$_4$)$_5$ (*Ln*: Y, Gd, Dy, Yb, Lu) und Ag$_3$Y(PS$_4$)$_2$. *Z. Anorg. Allg. Chem.* **2007**, *633*, 1633–1638. [CrossRef]
3. Deiseroth, H.-J.; Kong, S.-T.; Eckert, H.; Vannahme, J.; Reiner, C.; Zaiss, T.; Schlosser, M. Li$_6$PS$_5$*X*: A class of crystalline Li-rich solids with an unusually high Li$^+$ mobility. *Angew. Chem. Int. Ed.* **2008**, *47*, 755–758. [CrossRef] [PubMed]
4. Kraft, M.A.; Culver, S.P.; Calderon, M.; Böcher, F.; Krauskopf, T.; Senyshyn, A.; Dietrich, C.; Zevalkink, A.; Janek, J.; Zeier, W.G. Influence of Lattice Polarizability on the Ionic Conductivity in the Lithium Superionic Argyrodites Li$_6$PS$_5$*X* (*X* = Cl, Br, I). *J. Am. Chem. Soc.* **2017**, *139*, 10909–10918. [CrossRef] [PubMed]
5. Eulenberger, G. Die Kristallstruktur der Tieftemperaturmodifikation von Ag$_8$GeS$_6$. *Monatsh. Fr. Chem.* **1977**, *108*, 901–913. [CrossRef]

6. Minafra, N.; Kraft, M.A.; Bernges, T.; Li, C.; Schlem, R.; Morgan, B.J.; Zeier, W.G. Local Charge Inhomogeneity and Lithium Distribution in the Superionic Argyrodites Li_6PS_5X (X = Cl, Br, I). *Inorg. Chem.* **2020**, *59*, 11009–11019. [CrossRef]

7. Homma, K.; Yonemura, M.; Kobayashi, T.; Nagao, M.; Hirayama, M.; Kanno, R. Crystal structure and phase transitions of the lithium ionic conductor Li_3PS_4. *Solid State Ion.* **2011**, *182*, 53–58. [CrossRef]

8. Wu, Y.; Bensch, W. Structural diversity of rare earth and transition metal thiophosphates. *Cryst. Eng. Comm.* **2010**, *12*, 1003–1015. [CrossRef]

9. Klepov, V.V.; Pace, K.A.; Breton, L.S.; Kocevski, V.; Besmann, T.M.; zur Loye, H.C. Nearly Identical but Not Isotypic: Influence of Lanthanide Contraction on $Cs_2NaLn(PS_4)_2$ (Ln = La–Nd, Sm, and Gd–Ho). *Inorg. Chem.* **2020**, *59*, 1905–1916. [CrossRef]

10. Milot, S.; Wu, Y.; Näther, C.; Bensch, W.; Klepp, K.O. Two New Quaternary Thiophosphates with Pseudo One-dimensional Structures: Syntheses and Crystal Structures of $Cs_3Sm[PS_4]_2$ and $Rb_3Sm[PS_4]_2$. *Z. Anorg. Allg. Chem.* **2008**, *634*, 1575–1580. [CrossRef]

11. Wu, Y.; Bensch, W. Syntheses, structures, and spectroscopic properties of $K_9Nd[PS_4]_4$, $K_3Nd[PS_4]_2$, $Cs_3Nd[PS_4]_2$, and $K_3Nd_3[PS_4]_4$. *Inorg. Chem.* **2008**, *47*, 7523–7534. [CrossRef] [PubMed]

12. Evenson IV, C.R.; Dorhout, P.K. Thiophosphate phase diagrams developed in conjunction with the synthesis of the new compounds $KLaP_2S_6$, $K_2La[P_2S_6]_{0.5}[PS_4]$, $K_3La[PS_4]_2$, $K_4La_{0.67}[PS_4]_2$, $K_{9-x}La_{(1+x/3)}[PS_4]_4$ (x = 0.5), $K_4Eu[PS_4]_2$, and $KEuPS_4$. *Inorg. Chem.* **2001**, *40*, 2884–2891. [CrossRef] [PubMed]

13. Schoop, L.M.; Eger, R.; Kremer, R.K.; Kuhn, A.; Nuss, J.; Lotsch, B.V. Structural Stability Diagram of $ALnP_2S_6$ Compounds (A = Na, K, Rb, Cs; Ln = Lanthanide). *Inorg. Chem.* **2017**, *56*, 1121–1131. [CrossRef] [PubMed]

14. Aslani, C.K.; Breton, L.S.; Klepov, V.V.; zur Loye, H.C. A series of $Rb_4Ln_2(P_2S_6)(PS_4)_2$ (Ln = La, Ce, Pr, Nd, Sm, Gd) rare earth thiophosphates with two distinct thiophosphate units $P(V)S_4^{3-}$ and $P(IV)_2S_6^{4-}$. *Dalton Trans.* **2021**, *50*, 1683–1689. [CrossRef] [PubMed]

15. Goh, E.-Y.; Kim, E.-J.; Kim, S.-J. Structure Modification on Quaternary Rare Earth Thiophosphates: $NaYbP_2S_6$, $NaSmP_2S_6$, and $KSmP_2S_7$. *J. Solid State Chem.* **2001**, *160*, 195–204. [CrossRef]

16. Klepov, V.V.; Breton, L.S.; Pace, K.A.; Kocevski, V.; Besmann, T.M.; zur Loye, H.C. Size-Driven Stability of Lanthanide Thiophosphates Grown from an Iodide Flux. *Inorg. Chem.* **2019**, *58*, 6565–6573. [CrossRef]

17. Komm, T.; Schleid, T. $Li_9Nd_2[PS_4]_5$: A new lithium lanthanoid(III) thiophosphate(V). *J. Alloys Compd.* **2006**, *418*, 106–110. [CrossRef]

18. Lange, P.L.; Schleid, T. $Li_9Yb_2[PS_4]_5$ and $Li_6Yb_3[PS_4]_5$: Two lithium-containing ytterbium(III) thiophosphates(V) revisited. *Z. Naturforsch.* **2021**, *76b*, 281–291. [CrossRef]

19. Lange, P.L.; Komm, T.; Schleid, T. Two Hitherto Unknown Lithium Holmium(III) *Ortho*-Thiophosphates(V): $Li_9Ho_2[PS_4]_5$ and $Li_{15}Ho_7[PS_4]_{12}$. *Z. Anorg. Allg. Chem.* **2021**, *647*, 2113–2121. [CrossRef]

20. Lange, P.L.; Schleid, T. $Li_3La[PS_4]_2$: The First Lithium Lanthanum *Ortho*-Thiophosphate. *Eur. J. Inorg. Chem.* **2021**, *2021*, 3247–3254. [CrossRef]

21. Sheldrick, G.M. *SHELXS-97 and SHELXL-97: Programs for Solution and Refinement of Crystal Structures from X-ray Diffraction Data*; University of Göttingen: Göttingen, Germany, 1997.

22. Sheldrick, G.M. A short history of SHELX. *Acta Crystallogr.* **2008**, *A64*, 112–122. [CrossRef]

23. Sheldrick, G.M. Crystal structure refinement with *SHELXL. Acta Crystallogr.* **2015**, *C71*, 3–8.

24. Coelho, A.A. TOPAS and TOPAS-Academic: An optimization program integrating computer algebra and crystallographic objects written in C^{++}. *J. Appl. Crystallogr.* **2018**, *51*, 210–218. [CrossRef]

25. Cheary, R.W.; Coelho, A.A. Fundamental parameters approach to X-ray line-profile fitting. *J. Appl. Crystallogr.* **1992**, *1992*, 109–121. [CrossRef]

26. Cheary, R.W.; Coelho, A.A.; Cline, J.P. Fundamental Parameters Line Profile Fitting in Laboratory Diffractometers. *J. Res. Natl. Inst. Stand. Technol.* **2004**, *109*, 1–25. [CrossRef]

27. Le Bail, A.; Duroy, H.; Fourquet, J.L. Ab-initio structure determination of $LiSbWO_6$ by X-ray powder diffraction. *Mater. Res. Bull.* **1988**, *1988*, 447–452. [CrossRef]

28. Rietveld, H.M. A profile refinement method for nuclear and magnetic structures. *J. Appl. Crystallogr.* **1969**, *1969*, 65–71. [CrossRef]

29. Kubelka, P.; Munk, F.Z. Ein Beitrag zur Optik der Farbanstriche. *Technol. Phys.* **1931**, *12*, 593–601.

30. Chen, H.; Wong, L.L.; Adams, S. SoftBV—a software tool for screening the materials genome of inorganic fast ion conductors. *Acta Crystallogr.* **2019**, *75*, 18–33. [CrossRef]

31. Chen, H.; Adams, S. Bond softness sensitive bond-valence parameters for crystal structure plausibility tests. *IUCrJ* **2017**, *4*, 614–625. [CrossRef]

32. Momma, K.; Izumi, F.J. VESTA 3 for three-dimensional visualization of crystal, volumetric and morphology data. *J. Appl. Crystallogr.* **2011**, *44*, 1272–1276. [CrossRef]

33. Komm, T.; Gudat, D.; Schleid, T. Die Lanthanid(III)-*ortho*-Thiophosphate(V) vom Typ $M[PS_4]$ (M = La–Nd, Sm, Gd–Er): Synthese, Kristallstruktur und ^{31}P-NMR-Untersuchungen. *Z. Naturforsch. B* **2006**, *61*, 766–774. [CrossRef]

34. Fischer, R.X.; Tillmanns, E. The equivalent isotropic displacement factor. *Acta Crystallogr.* **1988**, *C44*, 775–776. [CrossRef]
35. Dieke, G.H. *Spectra and Energy Levels of Rare Earth Ions in Crystals*; Interscience Publishers, Wiley & Sons: New York, NY, USA, 1968.